Nanoscale

Effect of Reversible Dislocation-Based Deformation on Nanoparticle Strain at Failure

Journal:	*Nanoscale*
Manuscript ID	NR-ART-12-2024-005138.R1
Article Type:	Paper
Date Submitted by the Author:	12-Feb-2025
Complete List of Authors:	Zhang, Claire; University of California Merced, Prasad, Amit Kumar; University of Pittsburgh, Mechanical Engineering & Materials Science Liu, Ting; University of California Merced Jacobs, Tevis; University of Pittsburgh, Mechanical Engineering & Materials Science Martini, Ashlie; University of California Merced

Effect of Reversible Dislocation-Based Deformation on Nanoparticle Strain at Failure

Claire Zhang[1], Amit Kumar Prasad[2], Ting Liu[1], Tevis D.B. Jacobs[2], Ashlie Martini[1*]
[1)] Department of Mechanical Engineering, University of California, Merced, Merced, CA 95340, USA
[2)] Department of Mechanical Engineering and Materials Science, University of Pittsburgh, Pittsburgh, PA 15261, USA
[*] Corresponding author: amartini@ucmerced.edu

Key Words: Nanoparticles, Platinum, Deformation Mechanics, Reversible plasticity, Molecular dynamics simulations, In situ TEM testing

Abstract

Molecular dynamics simulations are used to isolate and quantify the reversible and irreversible mechanisms that contribute to deformation in platinum nanoparticles under compression. Quantitative analysis reveals how the nucleation and entanglement of dislocations can lead to reversible dislocation-based deformation. Simulations run at different temperatures and loading conditions show that the formation of entangled dislocations is more likely at higher temperatures and is facilitated by loading orientations where dislocations nucleate on intersecting slip planes. The presence of entangled dislocations increases the strain at failure due to the ability of those dislocations to accommodate strain reversibly. The results are corroborated by the observation of similar entangled dislocation loops during in situ compression experiments on nanoparticles of the same material. Overall, these findings provide insight into the role of dislocations in both reversible and irreversible deformation and their implications for nanoparticle stability and properties.

Introduction

Metal nanoparticles exhibit unique properties not found in their bulk counterparts. Due to their small size, metal nanoparticles have high surface activity, fewer structural defects, and diverse light-scattering and absorption properties. These properties of nanoparticles are leveraged in a variety of applications including catalysis**,** drug delivery, tribology, sensors, and solar power.[1–5] For optimal performance in these applications, metal nanoparticles must maintain specific sizes and shapes.[6–8] However, in practical conditions, metal nanoparticles are often subjected to mechanical forces such as compression, tension, or shear. These forces can deform the nanoparticles, altering their size and shape and consequently degrading their properties.[9]

Many prior studies on nanoparticle deformation have focused on the strength of nanoparticles in compression, particularly for very small particles in which defects are scarce.[10–12] In experiments, nanoindentation or atomic force microscopy can be employed to apply compressive strain to the particle, measure the resulting force, and extract parameters such as stress and strain.[11,13–16] The stress and strain at which deformation transitions from elastic (reversible) to plastic (irreversible) is critical as this comprises the nanoparticle's failure point, and is typically associated with the nucleation and propagation of dislocations through the particle. Structural changes caused by dislocations and the evolution of particle shape can be observed through in situ imaging using transmission electron microscopy (TEM) and scanning electron microscopy (SEM) during compression.[13,17–20] Such measurements can be complemented by

molecular dynamics (MD) simulations of nanoparticles, which offer the ability to track atomic movement and visualize deformation, often with higher precision than is achievable experimentally.[21,22] Similar to experimental data, simulation data can be used to generate force-distance or stress-strain curves from which transitions between reversible and irreversible deformation can be identified.[23–25] Furthermore, MD simulations have provided atomic-scale insight into dislocation nucleation and propagation in metal nanoparticles at a range temperatures.[22,24,26–31]

In both experiments and simulations, there is a challenge in analysis due to the mechanistic differences between nanoscale mechanical properties and conventional bulk properties. At the bulk scale, “reversible deformation” is typically associated with lattice compression, while “irreversible deformation” is typically associated with the nucleation and propagation of dislocations. However, in some cases, dislocation-based deformation can exhibit reversibility and recovery upon the removal of a load. Healing of plasticity was seen in nanoindentation experiments where defects remained localized within a gold film during loading and then retracted upon unloading.[32] Plastic recovery was also observed in nanoindentation of nanocrystalline gold and aluminum thin films after unloading and annealing.[33] Nanoindentation of thin plates of a titanium-tin alloy demonstrated that dislocation loops that nucleate but do not span the plate can retract upon load removal, contributing to pseudo-elastic deformation.[34] Low-cycle fatigue experiments with copper rods showed that dislocations with mixed edge and screw character can pile up during loading without exiting the structure and dissolve upon unloading.[35] Similarly, in situ experiments and MD simulations of twinned gold nanowires in tension revealed that dislocations can terminate at the twin boundaries and retract upon unloading.[36] It was shown that twinned silver and gold nanowires can be unstable due to unbalanced strain distributions, resulting in detwinning through strain relaxation.[19,37] Reversible dislocations can also be the result of a combination of surface and internal forces (image forces) that pull dislocations back out of the material when the load is removed, provided the dislocations do not exit the material during loading.[38,39] Finally, prior work by some of the present authors showed how reversible plasticity increases the size of the contact formed between a platinum surface and a platinum nanoscale probe. This increase was caused by dislocation loops nucleating at surface steps, allowing surface features to recede by one burgers vector such that the dislocations annihilated at the surface upon load removal.[40] These previous studies have confirmed that dislocation-based deformation can be reversible if conditions enable dislocations to remain in a material during loading in such that they can retract upon unloading, as may be the case with nanoparticles. Furthermore, MD simulation-based studies of compression of spherical aluminum, copper, and nickel nanoparticles showed that dislocation loops can nucleate from the edges of surface steps formed due to curvature and come together in a pyramid-like fashion without spanning the nanoparticle.[24,41,42] However, prior work has not explored how this dislocation pattern facilitates reversible plasticity, and its effect on the properties of nanoparticles in compression.

Here we use MD simulations to model the compression of platinum nanoparticles and isolate reversible dislocation-based deformation. Stress-strain curves were constructed, and the mechanisms of reversible and irreversible deformation were isolated and quantified. Specifically, the simulations were used to quantify deformation due to lattice compression and dislocations. Results showed that Pt nanoparticles can exhibit extensive reversible deformation due to the entanglement of dislocations. This finding was corroborated by real-time in situ compression testing of platinum nanoparticles, which demonstrated analogous dislocation patterns. Simulations were conducted at various temperatures and two loading orientations as a means of facilitating or suppressing different deformation mechanisms. Results demonstrated that the

likelihood of reversible deformation due to dislocations depends on temperature and loading orientation, and that this behavior directly influences the strain at failure of the nanoparticles.

Methods

Molecular Dynamics Simulation

MD simulations were conducted using Large-scale Atom/Molecular Massively Parallel Simulator (LAMMPS).[43] To create the Pt nanoparticle, a lattice structure from The Materials Project was imported into OVITO software and shaped into a 6-nm truncated octahedron with the [100] family of facets aligned with the x, y, and z-axes of the simulation box.[44,45] The size of the nanoparticle was defined as the diameter of the smallest sphere that fully encloses the particle. The truncated octahedron shape was chosen as it is the lowest-energy thermodynamics prediction of shape.[8] The embedded atom method (EAM) potential was used to describe atomic interactions, chosen based on its proven ability to accurately model the mechanical and surface properties of bulk and nanoscale platinum.[46,47]

The nanoparticle was first relaxed through an energy minimization process using the conjugate gradient method. Then the velocities were randomized following a Boltzmann distribution at temperatures from 300 to 900 K. Finally, the particles were equilibrated at each respective temperature with a Langevin thermostat until the potential energy reached a steady state. At each temperature, three distinct particle configurations were taken from different times during the equilibration process (after potential energy reached steady state) enabling three unique compression simulations at each temperature.

Following equilibration, the nanoparticle was oriented such that the [100] or [111] direction was oriented along the z-axis, as illustrated in Figure 1(a) for a particle oriented with respect to the [100] direction. Two parallel virtual walls with purely repulsive harmonic potentials were positioned above and below the nanoparticle. The harmonic potentials are described by $\mathrm{E} = \epsilon(r - r_c)^2; r < r_c$ where E is the energy of the wall-particle interaction, ϵ is the spring constant of the harmonic wall, r is the distance from an atom to the wall, and r_c is the cutoff distance at which the atom no longer interacts with the wall. A spring constant of 500 N/m and an interaction cutoff of 0.2 nm were used, based on a previous simulation study of nanoparticle compression.[46,47] These virtual walls were moved in along the z-axis towards the center of the nanoparticle, applying compressive forces perpendicular to the top and bottom facets of the nanoparticle. The walls were moved at a total rate of 1^{-7}/s or 1% per nanosecond to a maximum 10% strain, calculated as the ratio of the change in nanoparticle height at a given strain and the pre-compression height of the particle; a representative snapshot after compression is shown in Figure 1(b). The force on the walls, distance the walls have moved, and atom coordinates were recorded every 5 ps of simulation time. Stress was determined as the z-direction force on the walls divided by the total contact area of the walls to the top and bottom facets of the nanoparticle. LAMMPS simulation data was processed through OVITO for visual analysis of deformation mechanisms, as well as to track atomic movement and dislocation nucleation and progression.

Results and Discussion

Comparison of two cases to quantify reversible and irreversible deformation

Representative nanoparticle compression simulation snapshots along with stress-strain data from with a loading orientation of [100] run at 300 and 600K are shown in **Figure 1**. Similar results were obtained from simulations run at the same conditions but different initial atomic positions, as shown in **Figure S1**. At both temperatures, at low strain, the stress to compress the nanoparticle increased approximately linearly with increasing strain (Figure 1(c)). The rate of increase of stress with strain was lower at 600 K than at 300 K, which is attributable to increased thermal fluctuations decreasing the elastic constant.[51] However, both particles experienced their first significant stress drop around a similar strain, between 4.4% and 5.0%. This drop in stress typically associated with the release of elastic strain energy from the nucleation and propagation of a dislocation. [11,27] After the first drop, the stress increased linearly again, followed by more stress drops and further irreversible deformation.

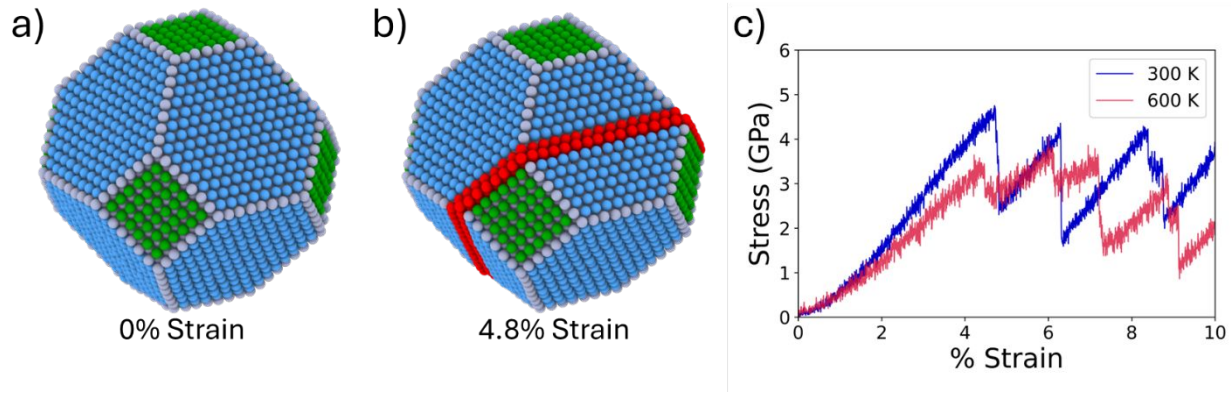

Figure 1: Compression along the [100] direction was performed on Pt nanoparticles and stress-strain curves were constructed from simulation data. A representative Pt nano particle at 300 K is shown at (a) 0% strain and (b) 4.8% strain with the [100] facets in green, [111] facets in blue, and atoms on the dislocation path in red. (c) Representative graphs of stress versus strain of compression at 300 and 600 K are shown in blue and red, respectively. Although high-temperature compression required less stress for the particle to deform to a given strain, the strain at which the load first dropped was similar at both temperatures.

To differentiate reversible and irreversible contributions in the compression simulations at 300 and 600 K, additional simulations were performed using a freeze-release process. During the compression phase, the nanoparticle's state (atom positions) was saved at various strain levels. Subsequent simulations were initiated from these recorded states. Each simulation involved holding the nanoparticle at a constant strain for 50 ps, followed by setting the temperature to 0 K (freeze), and then removing the compressive stress to allow the nanoparticle to relax, thus removing any reversible deformation (release). The particle's height, defined as the distance between its top and bottom facets, was measured after the release stage at each strain. Irreversible deformation was then quantified as the difference between the height at the start of the test (0% strain) and the height after the test (post-release); this can be recalculated after release for each of the various strain levels. This approach was verified by comparing the irreversible deformation obtained from the freeze-release method to the lattice shift associated with dislocations that pass completely through the particle (subsequently referred to as particle-spanning dislocations) for select cases (**Figure S2**). Reversible deformation was then determined

as the difference between the total deformation (measured from the positions of the compressing walls) and the irreversible deformation from the freeze-release method. This calculation was performed at 1% strain intervals between 0 and 10% strain and at 0.1% intervals near the transition from reversible to irreversible deformation.

Figure 2 shows the reversible and irreversible deformation determined by using the freeze-release method at 300 and 600 K. The onset of irreversible deformation was defined as the strain at which the total irreversible deformation became non-zero. The figure highlights the range between the earliest and latest onset of reversible deformation across all simulations conducted at each temperature. At higher temperatures, dislocation activity and the resulting irreversible deformation was expected to initiate at lower strains due to the weakening of atomic bonds from thermal expansion [29,52]. On this basis, the 600-K test would be expected to exhibit the onset of irreversible deformation at an earlier strain compared to 300 K. However, Figure 2 shows irreversible deformation was initiated earlier at 300 K (between 4.6 and 4.8% strain) than at 600 K (between 6.8 and 7.3% strain).

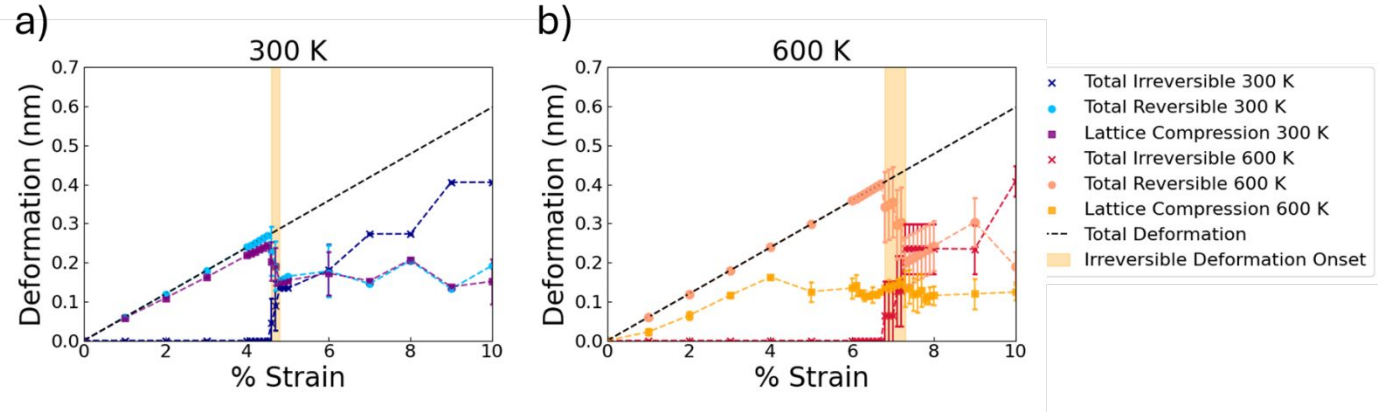

Figure 2: Strain at the onset of irreversible deformation is higher at 600 K compared to 300 K while 600 K also exhibits reversible deformation larger than deformation due to lattice compression. Reversible and irreversible contribution using the freeze-release method along with lattice compression calculated for (a) 300 K and (b) 600 K. The calculations were performed at smaller strain intervals near the transitions from reversible to irreversible. Error bars represent standard deviation of deformation from three independent simulations, colored dashed lines are used to guide the eye, dashed black lines represent the imposed deformation on the nanoparticle, and the ranges of the onset of irreversible deformation are shaded in beige. At 600K, the deformation due to lattice compression is much less than the total reversible deformation exhibited by the nanoparticle.

To understand the trend observed in the onset of irreversible deformation, it was necessary to first quantify the mechanisms of reversible deformation. In prior work, X-ray diffraction experiments quantify elastic deformation by measuring lattice compression, which can also be measured in simulation.[53,54] To mimic the X-ray diffraction experimental technique in simulation, lattice compression was determined based on the interplanar spacing of atoms in the direction of compression **(Figure S3**). Atoms in the center column of the nanoparticle directly between the facets in contact with the virtual wall were selected (Figure S3(a, b)) and their coordinates tracked through the compression process. Atoms surrounding dislocations were

excluded from this selection to isolate lattice compression from dislocation-induced motion, as dislocations locally distort the lattice away from an FCC structure. A 1D histogram of the z-direction distance between nearest neighbor atoms was generated for each timestep. This histogram was fitted with a polynomial curve, and the peak of the distribution was taken as the average interplanar spacing (Figure S3(c)). The change in average interplanar spacing was then multiplied by the number of layers of atoms in the nanoparticle in the direction of compression to find the total deformation due to lattice compression. This value was then subtracted from the value at 0% strain to find the magnitude of deformation due to lattice compression (Figure S3(d)). Lattice compression was analyzed at 1% strain intervals and at 0.1% intervals near the transition from reversible to irreversible deformation with the results also shown in Figure 2. At low strain, the deformation calculated from lattice compression is consistent with the reversible deformation found using the freeze-release technique and the total deformation. However, in the 600 K case after the strain at the first stress drop in Figure 1(c) (between 4.4 and 5.0% strain), the reversible deformation calculated directly from lattice compression is much lower than the total reversible deformation (Figure 2(b)).

From the freeze-release method, the onset of irreversible deformation was found to increase with temperature (Figure 2). Analysis of lattice compression at 600 K revealed that another reversible deformation mechanism, aside from lattice compression, must be contributing to the observed deformation (Figure 2(b)). These two findings prompted additional examination of dislocations during compression. **Figure 3** illustrates representative dislocation activity during compression at 300 and 600 K. The number of dislocations at each strain was tracked and graphed with the strain at the first drop in stress (from Figure 1(c)) and at the onset of irreversible deformation range (Figure 2). Dislocations behaved as expected in 300 K (Figure 3(a)), where the first detected dislocation activity occurred at a strain consistent with both the first drop in stress observed in the stress-strain data and the onset of irreversible deformation range identified using the freeze-release method. However, at 600 K (Figure 3(b)), while the initial drop in stress aligned with the first appearance of dislocations, the range for onset of irreversible deformation found from the freeze-release method occurred at much higher strain. This discrepancy suggested that some of the reversible deformation was attributable to dislocations, similar to reversible dislocation behavior observed in five-fold twinning, dislocation pile-up, and dislocation loops.[19,34–36,41]

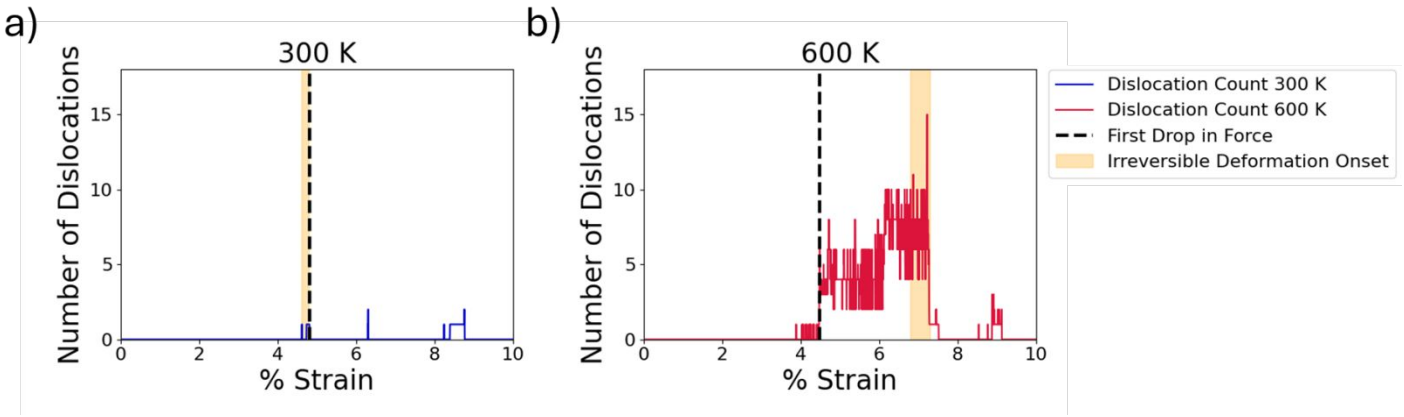

Figure 3: The strain at which dislocation activity begins is consistent with the strain at the first drop in stress but not necessarily with the onset of irreversible deformation.

Representative dislocation activity of (a) 300 K and (b) 600 K plotted against strain. Dislocation activity at both temperatures occurred around the same strain as the first drop in stress (black dashed lines). At 300 K, this strain was also consistent with the range of the onset of irreversible deformation observed from the freeze-release method (shaded beige ranges). However, at 600 K, the first drop in stress occurred at much lower strain than the onset of reversible deformation and significant dislocation activity was observed before any irreversible deformation, suggesting that the stress drop did not correspond to irreversible deformation.

Observation of reversible dislocation-based deformation in simulation and experiments

Dislocation nucleation and progression were examined visually in the simulations of nanoparticle compression at 600 K (**Figure 4**). Beginning at 4.0%, dislocations observed before the onset of irreversible deformation appeared as unstable segments nucleated at the edges of the nanoparticle, as illustrated in Figure 4(a). These dislocations developed into a persistent, entangled pyramidal pattern at 4.5% strain (Figure 4(b)), without forming any particle-spanning dislocations. This 4.5% strain corresponded to the first drop in stress (Figure 1(c)). Such entangled dislocations, also referred to as pyramid hillocks or pyramidal dislocation structures, have been documented in prior simulation literature for FCC metals.[55,56] In FCC lattice structures, dislocations are likely to nucleate from the edges of contact facets resulting in dislocations along (111) slip planes.[29,41] The pyramidal arrangement of intersecting (111) slip planes immobilized dislocation motion at the vertex of the pyramid, similar to the immobilization in Lomer-Cottrell locks.[55,56] In particular, the symmetry of the (111) slip planes when under [100] compression results in dislocations along all the slip planes reaching the same depth (distance from the surface) in the particle when they intersect. At an equal depth with mirrored symmetry, dislocations on each slip plane are subject to equal image forces.[57] This allows the dislocations comprising the entangled dislocation network to form such that no dislocation on any of the intersecting slip planes is favored, something possible because of the symmetry of the FCC lattice structure. One key difference between the entangled dislocations we observed and Lomer-Cottrell locks, however, is that the dislocations in this pyramidal arrangement of intersecting slip planes do not form a sessile dislocation. A Lomer-Cottrell lock involves dislocations on two (111) slip planes with a line intersection resulting in a sessile dislocation on the (100) plane which is not an FCC slip plane.[56,58] Instead, the pyramidal intersection of (111) slip planes results in entangled dislocations that are immobilized at a single point without also resulting in a sessile dislocation.

In our simulations, this was observed as an entangled dislocation network that intersected at the pyramid vertex where any individual dislocation was prevented from completely spanning the particle. Within this pyramidal structure, a small group of highly stable atoms can move along the intersecting slip planes (**Figure S4**). The dislocations comprising the entangled dislocation network were sufficiently close to their surfaces of nucleation that, if the compressive force were removed, these dislocations would be pulled back out of the material by dislocation image forces.[19,38,57] However, increased strain past a critical point disrupted the lattice sufficiently for one or more dislocations within the pyramidal network to span the particle, releasing strain energy. Figure 4(c) shows dislocations at 7.2% strain where the additional strain enabled one or more of the individual dislocations comprising the entangled dislocation network to break free and span the particle. This spanning dislocation marked the onset of irreversible deformation in the nanoparticle, consistent with freeze-release results that showed the onset of irreversible deformation occurred between 6.8 and 7.3% strain (Figure 2(c)).

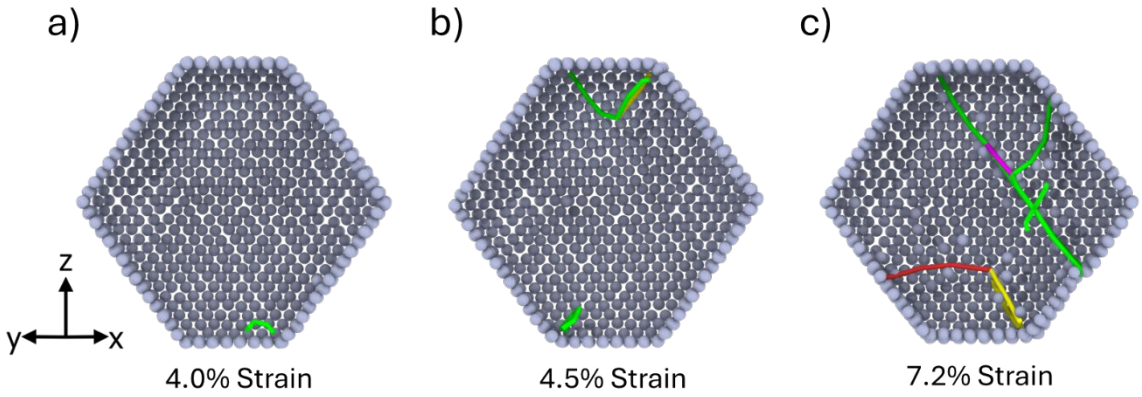

Figure 4: At 600 K, reversible entangled dislocation networks form before a particle-spanning dislocation causes irreversible deformation. At (a) 4.0% strain, dislocations nucleated along the edges of the particle but were unstable and frequently recede. At (b) 4.5% strain, entangled dislocations became a prominent, stable feature. At (c) 7.2% strain, a particle-spanning dislocation traveled through the particle resulting in the onset of irreversible deformation. The dislocation structures evolved from short dislocation segments nucleating from the surface to pyramidal entangled dislocations to system-spanning dislocation paths.

The entangled dislocations were corroborated by results from in situ TEM compression experiments on a truncated octahedron Pt nanoparticle. The methods for the compression experiments are described in Section S2 of the Supplemental Information. The real-time video of the compression (**Video S1**) is also available in the Supplemental Information and representative images are shown in **Figure 5**. The initial shape of the particle was a modified truncated octahedron, as shown in Figure 5(a); this shape is faceted, but does not quite correspond to the lowest-energy thermodynamic prediction of shape, as discussed extensively in Ding et al.[8] As compression was applied, dislocations initiated from the top surface of the particle and an entangled dislocation was observed (Figure 5(b), arrow). The inset image is color inverted and is zoomed closer in to highlight the dislocation loop. Dislocations initiate and propagate along the four {111} facets. Then, the interaction of these dislocations resulted in an entangled dislocation, according to equation: $\frac{1}{6}[\bar{1}2\bar{1}] + \frac{1}{6}[1\bar{1}2] \rightarrow \frac{1}{6}[011]$.[41] The presence of bands of contrast (indicated by an arrow) confirms the formation of entangled dislocations, as shown in Figure 5(b). Then, two entangled dislocations were formed with further compression (Figure 5(c)). Finally, upon unloading, the entangled dislocation network dissociated, as shown in Figure 5(d), exhibiting reversible plasticity.

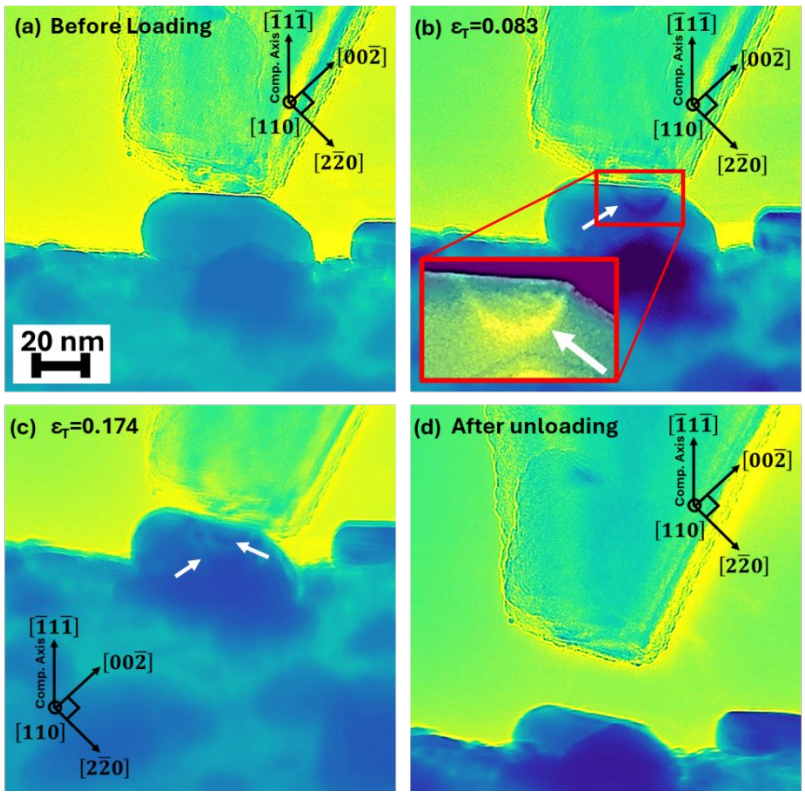

Figure 5: In situ compression was performed on an 80±10 nm platinum nanoparticle revealing entangled dislocation patterns. (a-c) entangled dislocation pyramidal formation and (d) dissociation after unloading. Arrows indicate the location of pyramidal entangled dislocations. Inset image in (b) highlights the entangled dislocation loop with inverted colors. See Video S1 of the supplementary materials for a visual representation of the nanoparticle deformation process.

The reversible deformation seen in experiments occurred through a network of two entangled dislocations, which differed from the single (pyramid-shaped) entangled dislocation seen in our simulations. This difference in mechanism can be explained by the difference in nanoparticle size, 6 nm in simulations and 80 nm in experiments, and slight differences in loading conditions. Smaller nanoparticles have fewer line edges on the surface, which result in fewer overall dislocations inside the material at any specific moment. Also, the symmetry and controlled loading of the simulations increased the likelihood that dislocations would enter the material at the same moment and at the right orientation to entangle. In experiments, where symmetry of orientation and loading is less controlled, the entanglements still form, but it is more of a stochastic process, and is more likely to occur at a moment when several dislocations are acting concurrently.[41] Regardless, both simulations and experiments exhibit the same key features where dislocations nucleate at the edges of the contact during loading and then lock, remaining in the nanoparticle until the load is removed at which point they retract from the particle. The consistency supports the physical realism and relevance of the simulations that showed reversible deformation of nanoparticles in compression. Based on this, the simulations were analyzed further to quantify the magnitude of deformation due to entangled dislocations and their effect on ultimate properties.

We quantified the contribution of entangled dislocations to reversible deformation in simulations by comparing the positions of adjacent atoms on either side of the pyramidal slip plane boundary. The z-direction spacing was subtracted from the initial spacing at 0% strain to find the deformation due to entangled dislocations (Figure S4(b, c)). **Figure 6** shows the contribution of all three deformation mechanisms to overall deformation at 300 and 600 K. The contribution of spanning dislocations was calculated from the irreversible deformation determined by the freeze-release method, the contribution of lattice compression was determined by calculating interatomic spacing, and the contribution of entangled dislocations was determined by comparing the positions of atoms inside and outside of the dislocation network slip plane boundaries. At 300 K, the total deformation can be attributed to lattice compression and spanning dislocations, with no significant contribution from entangled dislocations. In contrast, at 600 K, a notable contribution from entangled dislocations was observed, consistent with the dislocation activity in Figure 4(b). The initial drop in stress around 4.5% strain (Figure 1(c)) corresponded with a persistent entangled dislocation network, while the second drop in stress around 7.2% strain corresponded to the appearance of the first spanning dislocation. This additional contribution from entangled dislocations explains the reversible deformation that was unaccounted for in Figure 3.

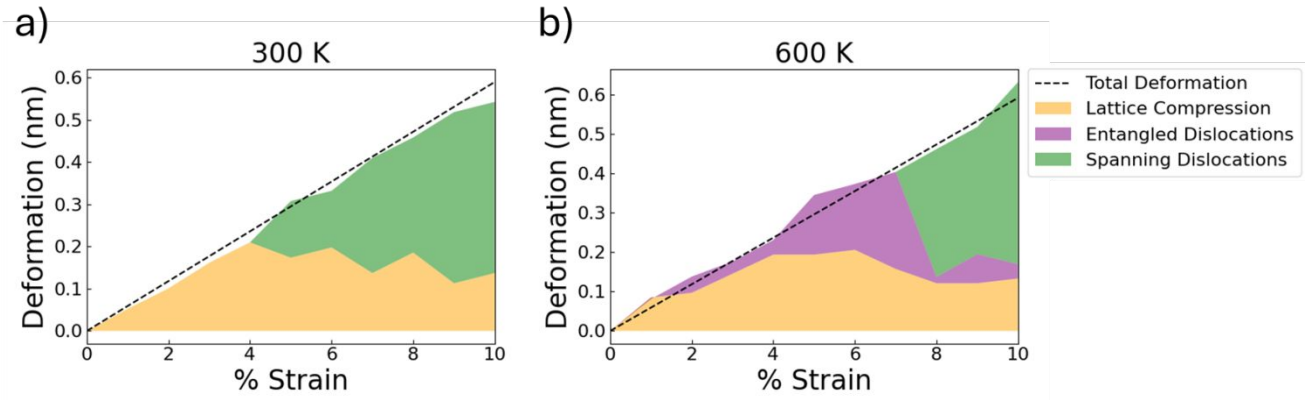

Figure 6: Entangled dislocations account for the reversible deformation that is not due to lattice compression. Representative stacked plots of the contribution of individual deformation mechanism at (a) 300 K and (b) 600 K. The dashed line represents the imposed deformation on the nanoparticle, while yellow represents lattice compression, purple represents entangled dislocations, and green represents spanning dislocations. At 300 K, there was no contribution from entangled dislocations whereas, at 600 K, a significant contribution from entangled dislocations was observed. Deformation contribution plots from two other independent simulations at each temperature are shown in **Figure S5** and exhibit the same trends.

Effect of reversible deformation on strain at failure

We identified a significant contribution to reversible deformation from entangled dislocations at 600 K (Figure 6(b)). Additionally, the onset of irreversible deformation as determined by the freeze-release method occurred at a higher strain at 600 K than at 300 K (Figure 2). This suggests that the presence of entangled dislocations delay the onset of irreversible deformation, which may affect the failure point of the particle. To test this hypothesis,

we conducted simulations at other temperatures and with compressive loading in the [111] direction. **Figure 7** shows the frequency at which entangled dislocations occurred for different temperature and loading direction cases. For loading in [111] direction, no entangled dislocations were observed at any temperature. This is because the <111> facet of the particle is a hexagon such that compression in the [111] direction results in possible dislocations on opposing edges having (100) and (111) slip planes. As the stacking fault energy of the (111) plane is lower than that of the (100) plane, dislocation motion is more likely to along the (111) than the (100) plate such that there is no possibility for dislocations that nucleate from opposing edges to interlock.[59] The lack of symmetry of the intersecting slip planes in the [111] direction and the resulting uneven image forces prevent entangled dislocations from forming.[41,57] For [100] loading, **Figure 7(a)** shows that the likelihood of entangled dislocations was temperature dependent. Particularly, there were no entangled dislocations at 300 K and entangled dislocations always occurred at temperatures of 400 K and higher. Between those temperatures, the likelihood of entangled dislocations increased with increasing temperature. This temperature dependence is attributable to the fact that dislocation nucleation rates increase with temperature.[31] At higher temperatures, this results in higher likelihood of dislocations occurring on intersecting slip planes simultaneously, so that when the dislocations propagate, they entangle.

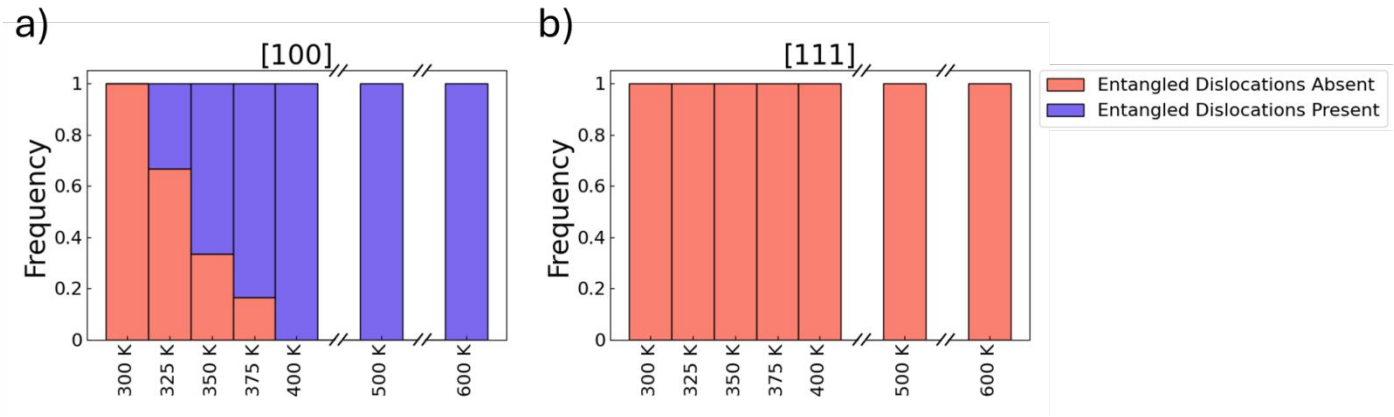

Figure 7: Likelihood of entangled dislocations increases with temperature in [100] compression while no entangled dislocations are exhibited in [111] compression. Histograms of the frequency at which entangled dislocations occurred in simulations in the 300 to 600 K range for (a) [100] compression and (b) [111] compression. Orange and violet represent entangled dislocations being absent and present, respectively.

Figure 8 shows the stress at failure from compression simulations along the [100] or [111] direction at temperatures ranging from 300 to 900 K. The results are categorized based on the presence or absence of entangled dislocations at each temperature and compression direction. For both [100]-oriented compression (Figure 8(a)) and [111]-oriented compression (Figure 8(b)), stress at failure decreased with increasing temperature. This trend is emphasized using dashed lines to guide the eye with shaded regions corresponding to the 95% confidence and prediction intervals. A decrease in stress at failure with increasing temperature was observed in previous studies of FCC metals and was attributed to an increase in dislocation activity at higher temperature.[29–31] However, the presence or absence of entangled dislocations did not significantly affect the stress at failure. Specifically, for loading in the [100] direction from 325 to 375 K, the difference in stress at failure between simulations with and without entangled dislocations was not significant (Figure 8(a)).

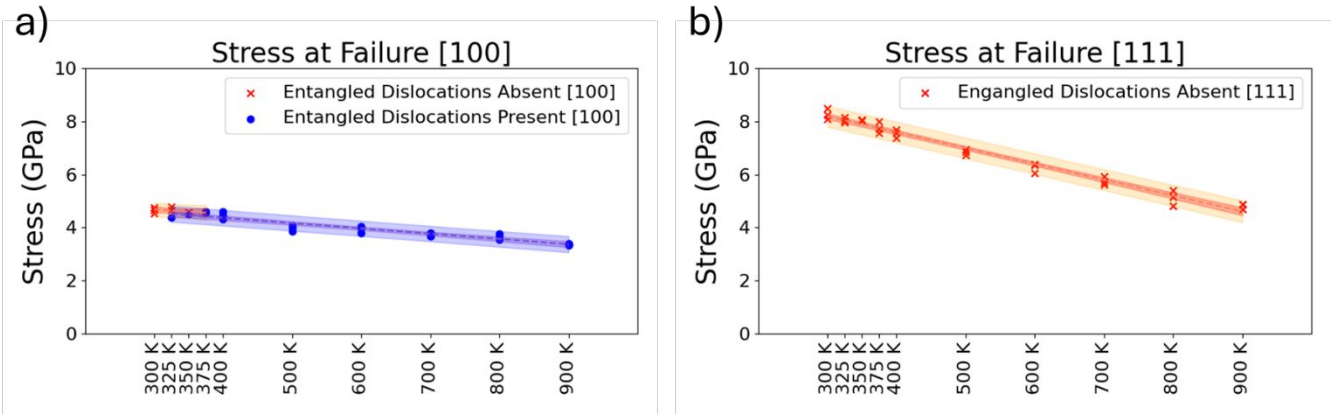

Figure 8: Stress at failure decreases with increasing temperature but is not affected by the presence or absence of reversible dislocations. Stress at failure is determined based on the point at which the first particle-spanning dislocation occurs during compression in the (a) [100] direction or the (b) [111] direction. Colored dashed lines are used to guide the eye with the darker shaded area representing a 95% confidence interval and lighter shaded area representing a 95% prediction interval. Orange and violet color schemes are used for cases where entangled dislocations are absent and present, respectively.

Figure 9 shows the strain at failure from compression simulations along the [100] or [111] direction at temperatures ranging from 300 to 900 K, categorized based on the presence or absence of entangled dislocations at each temperature and compression direction. Figure 9(a) and Figure 9(b) show that strain at failure varies little with temperature for both compression directions, as evidenced by the 95% confidence and prediction intervals. This result aligns with prior research suggesting that strain at failure is relatively independent of temperature.[18,60] However, in contrast to stress at failure, strain at failure was affected by entangled dislocations. In cases where entangled dislocations were present ([100] loading at higher temperatures), the 95% prediction interval for strain at failure was 6.0-7.8%; this is significantly higher than a 95% prediction interval of 4.2-5.4% in cases where entangled dislocations were absent (Figure 8(a)). In [111] compression, where no entangled dislocations formed, the 95% prediction interval for strain at failure was 6.1-8.6% (Figure 8(b)). Thus, the presence of entangled dislocations increases strain at failure.

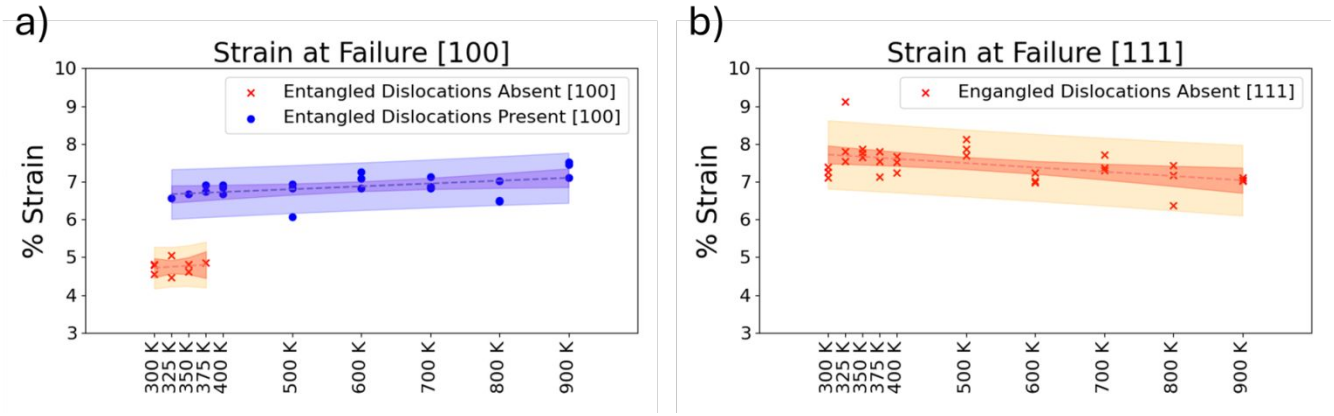

Figure 9: Strain at failure is higher in cases where entangled dislocation occurred ([100] loading at higher temperatures) but exhibits a statistically insignificant change with temperature. (a, b) strain at failure determined based on the point at which the first particle-spanning dislocation occurs during compression in the (a) [100] direction or the (b) [111] direction. Colored dashed lines are used to guide the eye with the darker shaded area representing a 95% confidence interval and lighter shaded area representing a 95% prediction interval. Orange and violet color schemes are used for cases where entangled dislocations are absent and present, respectively.

In our simulations, a drop in stress (Figure 1(c)) could correspond to either a spanning or entangled dislocation. When the dislocation was a spanning dislocation, the drop in stress was associated with irreversible deformation and material failure. When the dislocation was an entangled dislocation, the stress dropped since the entangled dislocation was able to accommodate strain without failure **(Figure S6**). Additional strain caused stress to increase again until the threshold for dislocation propagation was reached, and the entangled dislocation evolved into a spanning dislocation leading to irreversible deformation and failure. The higher strain necessary for dislocation propagation after an entangled dislocation is consistent with previously reported Lomer-Cottrel lock behavior in requiring additional strain to break the entangled dislocation lock.[61] However, the presence or absence of entangled dislocations did not affect stress at failure and did not follow Lomer-Cottrel lock behavior in requiring additional stress to break the lock.[58] This may be because the pyramidal entangled dislocation formation did not result in sessile dislocations as traditional Lomer-Cottrell locks would.[56,58] Thus, the presence of an entangled dislocation did not affect stress at failure but increased strain at failure since higher strain was required to reach the same stress threshold for dislocation propagation.

Conclusion

In summary, we investigated the deformation behavior of Pt nanoparticles through MD simulations. Compression simulations were conducted with varied temperature and loading direction to construct stress-strain curves and to isolate the contributions of three different deformation mechanisms: lattice compression, entangled dislocations, and particle-spanning dislocations. The contributions of each deformation mechanism to the total strain were quantified. Lattice compression alone could not account for all reversible deformation, instead significant dislocation activity and a drop in stress was observed when deformation was still fully reversible.

Entangled dislocations are then shown to provide a source of reversible deformation and significantly delay the onset of irreversible deformation. These entangled dislocations exhibited Lomer-Cottrel lock-like behavior that was corroborated by in situ compression tests from which we observed the formation of entangled dislocation structures in a platinum nanoparticle. Finally, analysis of simulations at multiple temperatures and loading directions showed that entangled dislocations were more likely at higher temperatures and loading directions where dislocations have a greater probability of nucleating on intersecting slip planes. These entangled dislocations are encouraged by the symmetrical nature of the FCC lattice resulting in mirrored (111) slip planes during [100] compression and multiple dislocation nucleation events on mirrored slip planes. The symmetry ensures that no one slip plane is favored for dislocation motion, maximizing the probability that dislocations lock when they intersect. This quantification of the effect of entangled dislocations on reversible and irreversible deformation provides insight into nanoparticle deformation mechanisms during compression. As the entangled dislocation phenomenon is dependent on geometry and symmetry, other FCC metals with geometries and compression directions that encourage symmetrical slip planes are also likely to produce entangled dislocations, suggesting the findings may be more broadly applicable. Future studies may explore other nanoparticle materials, shapes, and sizes, using the computational framework developed here. We also analyzed the effect of reversible plasticity on the ultimate properties of the nanoparticle and demonstrated that entangled dislocations increase the strain at failure of the nanoparticle. This observation suggests the possibility of using dislocation entanglement to manipulate material properties, e.g., increasing temperature to encourage dislocation entanglement which will increase strain at failure. Understanding the conditions that enable reversible plasticity and the implications for material properties can ultimately enable nanoparticles with mechanical robustness that can be used for a range of potential applications.

Conflict of Interest

The authors declare no conflict of interest.

Data Availability

The input files for LAMMPS Molecular Dynamics simulations have been uploaded to Open Science Framework: https://osf.io/uj4tm/.

Acknowledgements

The authors acknowledge the support of the U.S. Department of Energy, Office of Science, Office of Basic Energy Sciences. The Award number is DE–SC0021155. The authors also acknowledge the use of Nanoscale Fabrication and Characterization Facility in the Gertrude E. & John M. Petersen Institute of Nanoscience and Engineering located in Swanson School of Engineering.

1 J. G. Smith, J. A. Faucheaux and P. K. Jain, *Nano Today*, 2015, **10**, 67–80.
2 M. J. Ndolomingo, N. Bingwa and R. Meijboom, *J. Mater. Sci.*, 2020, **55**, 6195–6241.
3 V. Vio, M. J. Marchant, E. Araya and M. K. Kogan, *Curr. Pharm. Des.*, 2017, **23**, 1916–1926.
4 M. Akbulut, *J. Powder Met. Min.*, , DOI:10.4172/2168-9806.1000e101.
5 R. Ding, N. C. Miller, K. M. Woeppel, X. T. Cui and T. D. B. Jacobs, *Langmuir*, 2022, **38**, 7512–7521.
6 M. Rai, A. P. Ingle, S. Birla, A. Yadav and C. A. D. Santos, *Crit. Rev. Microbiol.*, 2015, 1–24.
7 R. M. Rioux, H. Song, P. Yang and G. A. Somorjai, in *Metal Nanoclusters in Catalysis and Materials Science*, Elsevier, 2008, pp. 149–166.
8 R. Ding, I. M. Padilla Espinosa, D. Loevlie, S. Azadehranjbar, A. J. Baker, G. Mpourmpakis, A. Martini and T. D. B. Jacobs, *Nanoscale Adv.*, 2022, **4**, 3978–3986.
9 X. Wang, S. Zheng, S. Shinzato, Z. Fang, Y. He, L. Zhong, C. Wang, S. Ogata and S. X. Mao, *Nat. Commun.*, 2021, **12**, 5237.
10 D. Mordehai, O. David and R. Kositski, *Adv. Mater.*, 2018, **30**, 1706710.
11 D. Mordehai, S.-W. Lee, B. Backes, D. J. Srolovitz, W. D. Nix and E. Rabkin, *Acta Mater.*, 2011, **59**, 5202–5215.
12 R. Maaß, L. Meza, B. Gan, S. Tin and J. R. Greer, *Small*, 2012, **8**, 1869–1875.
13 J. Zimmerman, A. Bisht, Y. Mishin and E. Rabkin, *J. Mater. Sci.*, 2021, **56**, 18300–18312.
14 S. Azadehranjbar, R. Ding, I. M. Padilla Espinosa, A. Martini and T. D. B. Jacobs, *ACS Nano*, 2023, **17**, 8133–8140.
15 R. Ding, S. Azadehranjbar, I. M. Padilla Espinosa, A. Martini and T. D. B. Jacobs, *ACS Nano*, 2024, **18**, 4170–4179.
16 H. Li, Y. Han, T. Duan and K. Leifer, *Appl. Phys. Lett.*, 2019, **115**, 053104.
17 J. Sun, L. He, Y.-C. Lo, T. Xu, H. Bi, L. Sun, Z. Zhang, S. X. Mao and J. Li, *Nat. Mater.*, 2014, **13**, 1007–1012.
18 T. Fedyaeva, S. Mathesan, A. Bisht, Z. Liang, D. Mordehai and E. Rabkin, *Acta Mater.*, 2023, **261**, 119417.
19 M. Song, J. Cui, C. Ophus, J. Lee, T. Yan, K. A. Fichthorn and D. Li, *Nano Lett.*, 2024, **24**, 1153–1159.
20 J. E. Norman, X. Wang, A. D. Dupuy and J. M. Schoenung, *Appl. Phys. Lett.*, , DOI:10.1063/5.0211263.
21 P. Tian, *Annu. Rep. Sect. C (Phys. Chem.)*, 2008, **104**, 142.
22 J. Amodeo and L. Pizzagalli, *C. R. Phys.*, 2021, **22**, 35–66.
23 I. M. Padilla Espinosa, S. Azadehranjbar, R. Ding, A. J. Baker, T. D. B. Jacobs and A. Martini, *Appl. Phys. Lett.*, , DOI:10.1063/5.0078035.
24 A. M. Goryaeva, C. Fusco, M. Bugnet and J. Amodeo, *Phys. Rev. Mater.*, , DOI:10.1103/physrevmaterials.3.033606.
25 I. M. Padilla Espinosa, T. D. B. Jacobs and A. Martini, *Nanoscale Res. Lett.*, 2022, **17**, 96.
26 S. Roy, R. Gatti, B. Devincre and D. Mordehai, *Comput. Mater. Sci.*, 2019, **162**, 47–59.
27 Y. Feruz and D. Mordehai, *Acta Mater.*, 2016, **103**, 433–441.
28 J. A. de la Rosa Abad, A. Londoño-Calderon, E. M. Bringa, G. J. Soldano, S. A. Paz, U. Santiago, S. J. Mejía-Rosales, M. J. Yacamán and M. M. Mariscal, *J. Phys. Chem. C*, 2021, **125**, 25298–25306.
29 S. Brochard, P. Hirel, L. Pizzagalli and J. Godet, *Acta Mater.*, 2010, **58**, 4182–4190.
30 D. Chachamovitz and D. Mordehai, *Sci. Rep.*, , DOI:10.1038/s41598-018-21868-y.
31 T. Zhu, J. Li, A. Samanta, A. Leach and K. Gall, *Phys. Rev. Lett.*, , DOI:10.1103/physrevlett.100.025502.
32 G. L. W. Cross, A. Schirmeisen, P. Grütter and U. T. Dürig, *Nat. Mater.*, 2006, **5**, 370–376.
33 J. Rajagopalan, J. H. Han and M. T. A. Saif, *Science*, 2007, **315**, 1831–1834.
34 J. P. Cui, Y. L. Hao, S. J. Li, M. L. Sui, D. X. Li and R. Yang, *Phys. Rev. Lett.*, 2009, **102**, 045503.
35 C. Kirchlechner, P. J. Imrich, W. Liegl, J. Pörnbacher, J.-S. Micha, O. Ulrich and C. Motz, *Acta Mater.*, 2015, **94**, 69–77.
36 Q. Qin, S. Yin, G. Cheng, X. Li, T.-H. Chang, G. Richter, Y. Zhu and H. Gao, *Nat. Commun.*, 2015, **6**, 5983.
37 M. Song, Z. Wu, N. Lu and D. Li, *Chem. Mater.*, 2019, **31**, 842–850.
38 P. Khanikar, A. Kumar and A. Subramaniam, *Philos. Mag. (Abingdon)*, 2011, **91**, 730–750.
39 B. Q. Li, M. L. Sui, B. Li, E. Ma and S. X. Mao, *Phys. Rev. Lett.*, 2009, **102**, 205504.
40 S. B. Vishnubhotla, R. Chen, S. R. Khanal, A. Martini and T. D. B. Jacobs, *Nanotechnology*, 2019, **30**, 035704.
41 S. Bel Haj Salah, C. Gerard and L. Pizzagalli, *Comput. Mater. Sci.*, 2017, **129**, 273–278.
42 B. Jianjun and G. Wang, *Journal of Computational and Theoretical Nanoscience*, , DOI:10.1166/jctn.2013.3201.
43 A. P. Thompson, H. M. Aktulga, R. Berger, D. S. Bolintineanu, W. M. Brown, P. S. Crozier, P. J. in 't Veld, A. Kohlmeyer, S. G. Moore, T. D. Nguyen, R. Shan, M. J. Stevens, J. Tranchida, C. Trott and S. J. Plimpton, *Comput. Phys. Commun.*, 2022, **271**, 108171.
44 P. Shyue, G. Ong, W. Hautier, W. D. Chen, S. Richards, S. Dacek, D. Cholia, D. Gunter, G. Skinner and K. A. Ceder, *Commentary: The Materials Project: A materials genome approach to accelerating materials innovation Anubhav Jain*, .
45 A. Stukowski, *Modelling Simul. Mater. Sci. Eng.*
46 I. M. Padilla Espinosa, T. D. B. Jacobs and A. Martini, *J. Chem. Theory Comput.*, 2021, **17**, 4486–4498.
47 X. W. Zhou, H. N. G. Wadley, J.-S. Filhol and M. N. Neurock, *Phys. Rev. B Condens. Matter Mater. Phys.*, , DOI:10.1103/physrevb.69.035402.
48 J. E. Sader, J. W. M. Chon and P. Mulvaney, *Rev. Sci. Instrum.*, 1999, **70**, 3967–3969.
49 A. Kosinova, O. Kovalenko, L. Klinger and E. Rabkin, *Acta Mater.*, 2015, **83**, 91–101.

50 M. Bechelany, X. Maeder, J. Riesterer, J. Hankache, D. Lerose, S. Christiansen, J. Michler and L. Philippe, *Cryst. Growth Des.*, 2010, **10**, 587–596.
51 Y. A. Chang and L. Himmel, *J. Appl. Phys.*, 1966, **37**, 3567–3572.
52 S. Ryu, K. Kang and W. Cai, *J. Mater. Res.*, 2011, **26**, 2335–2354.
53 S.-I. Karato, *Phys. Rev. B Condens. Matter Mater. Phys.*, , DOI:10.1103/physrevb.79.214106.
54 L. Li, D. J. Weidner, J. Chen, M. T. Vaughan, M. Davis and W. B. Durham, *J. Appl. Phys.*, 2004, **95**, 8357–8365.
55 V. Bulatov, F. F. Abraham, L. Kubin, B. Devincre and S. Yip, *Nature*, 1998, **391**, 669–672.
56 J. P. Hirth and J. Lothe, *Theory of Dislocations*, John Wiley & Sons, Nashville, TN, 2nd edn., 1982.
57 G. Huang, B. Svendsen and Z. Lu, *Acta Mech. Solida Sin.*, 2009, **22**, 436–442.
58 D. Rodney and R. Phillips, *arXiv [cond-mat.mtrl-sci]*, 1998.
59 A. M. Cuitiño, *Mater. Sci. Eng. A Struct. Mater.*, 1996, **216**, 104–116.
60 E. Rabkin and D. J. Srolovitz, *Nano Lett.*, 2007, **7**, 101–107.
61 L. Wang, J. Teng, X. Sha, J. Zou, Z. Zhang and X. Han, *Nano Lett.*, 2017, **17**, 4733–4739.

Data Availability

The input files for LAMMPS Molecular Dynamics simulations have been uploaded to Open Science Framework: https://osf.io/uj4tm/.